Statistics of shock waves in a two-dimensional granular flow

S. Hørlück and P. Dimon
The Center for Chaos and Turbulence Studies, The Niels Bohr Institute, Blegdamsvej 17, DK-2100 Copenhagen Ø, Denmark
(Received 22 January 1999)

We have investigated the dynamics of shock waves in a single layer of uniform balls in a small-angle two-dimensional funnel. When the funnel half-angle $0° \lesssim \beta \lesssim 2°$, the flow is intermittent and kinematic shock waves are observed to propagate against the flow. We have used fast video equipment and image analysis methods to study the statistics of the shock waves. It is found that their speed and frequency increase with the distance from the outlet. In particular, the shock speed scales as the ratio of the local funnel width to the width of the funnel outlet. Various kinds of interactions between shock waves are observed, including repulsion. New shock waves are only created at those sites where a close-packed triangular packing of the monodisperse balls fits across the funnel. [S1063-651X(99)01307-0]

PACS number(s): 45.70.Mg

I. INTRODUCTION

Flowing granular matter exhibits a variety of unusual phenomena [1–3]. It is known, for example, that the flow rate in an hourglass is essentially independent of the head of the granular material [4]. Furthermore, the flow is not necessarily steady and there can be fluctuations in the flow rate. In particular, in an earlier work, Veje and Dimon (VD) found kinematic shock waves in a two-dimensional flow of monodisperse brass balls in a small-angle funnel [5].

In this work, the dynamics of these shock waves are studied using fast video equipment [6]. Qualitative studies were made of the general phenomenology. Image analysis tools were used for quantitative analysis of the statistics of shock wave speeds and frequencies. The paper is structured as follows. In Sec. II we review previous work in which density waves were present. In Sec. III we describe the experimental setup. In Sec. IV we discuss the general behavior. In Sec. V we outline the methods used to identify shock waves. In Sec. VI we present the shock wave statistics and in Sec. VII we show how some of the data can be rescaled. In Sec. VIII we discuss shock wave creation. In Sec. IX we describe shock wave interactions. In Sec. X we summarize our results.

II. DENSITY WAVES IN GRANULAR FLOWS

We will briefly review some pertinent earlier work on granular flow in which density waves have been observed.

A. The hourglass and pipe flow

The hourglass is probably the oldest known technical application of granular flow. (See Mills *et al.* [7] for a history.) It is desirable that real hourglasses have steady, reproducible flow rates, and thus their designs are aimed at avoiding intermittent flow. By making various adjustments to grain properties or geometry, such as prolonging the stem of the hourglass, intermittent flow regimes can be obtained [8–11]. The resulting density fluctuations usually take the form of slugs (regions with high density and low velocity) separated by low density regions of grains in free fall [8]. It has been shown by Wu *et al.* [9] that sand flow between sealed containers (in a nondisturbed flow) exhibits flow intermittency as a consequence of counterflow of the interstitial fluid and is absent in flow between unsealed containers.

Experimental versions of the ''long stem'' hourglass typically consist of a long pipe connecting reservoirs. The flow rate at the inlet or outlet may often be controlled [12,13] or the interstitial air may be replaced by denser fluids [13]. Raafat *et al.* [12] achieve propagating slugs by controlling the pipe outlet size in an open system. Thus density waves may also be achieved by shifting the balance between inflow and outflow when there is no counterflow of the interstitial fluid.

B. Funnel flow

If a granular material in a box is drained out through a central aperture in the bottom, the grains will flow in some funnel-shaped region above the aperture defined by the angle of approach β_{cr} [1]. Granular matter outside this region (i.e., closer to the wall) does not flow. A granular container designed to be emptied by gravity through a bottom aperture should therefore be funnel-shaped at the bottom with a funnel half-angle $\beta < \beta_{cr}$ (and preferably have vertical walls further up to avoid nonflowing zones far from the aperture).

Large scale granular containers (silos) are typically constructed according to this design. Since a flow may cause dangerously large pressure fluctuations at the inner walls of silos, flow in funnels is a field of considerable technological interest. The advantage of having a flow confined by well-defined walls instead of some possibly ill-defined border between flow and stagnation also makes the funnel flow attractive from a modeling point of view. Consequently funnel flows are of considerable experimental [1,7,14–17] and theoretical [1,18–20] interest. Often the funnels studied in experiments are quasi-two-dimensional in order to allow visual or x-ray studies of the internal flow [15–17].

Several experimenters have found density waves in such geometries. Lee *et al.* [15] describes them as traveling downwards when $\beta = 30°$. Michalowski [16] observes them moving upwards when $\beta = 15°$. Baxter *et al.* [17] found that density waves propagated upwards for $\beta > 17.5°$ and downwards for $\beta < 17.5°$ in a granular matter composed of rough sand.

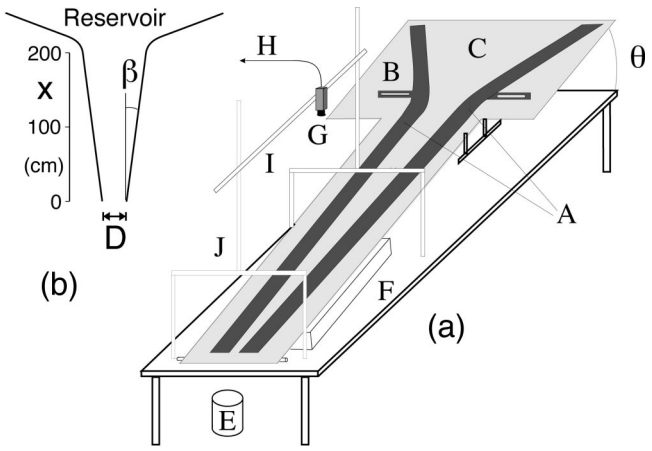

FIG. 1. (a) Schematic of the experiment. (b) Parameters of the funnel geometry.

Density waves were absent using smooth sand but a mixture with at least 22% rough sand reestablished them [14]. These apparently contradictory results seem to suggest that other parameters, such as the roughness of the walls and grains, also play an important role.

III. EXPERIMENTAL SETUP

A. Flow system

The granular matter used throughout the experiment was composed of approximately 50 000 brass balls. Each ball had a diameter of 3.18 mm (1/8 in.), a sphericity of 0.2%, and a measured average weight of 0.14 g. The angle of repose has been estimated to be $\sim 15°$ (from VD [5]). The coefficient of restitution was measured to have a lower limit of $\epsilon \simeq 0.74 \pm 0.02$. Brass balls were chosen to avoid magnetization effects. Before each series of experiments the balls were cleaned in water and detergent followed by isopropanol.

The structure of the experiment is shown in Fig. 1(a). The brass balls roll in one layer between 3.45 mm high aluminum walls (A) resting on a coated Lexan plane (B). (Lexan is harder than Plexiglas.) The aluminum walls have 200-cm-long straight sections which then open smoothly at the top forming a reservoir area (C). The straight sections of the aluminum walls form a long narrow funnel and they may be moved to vary the outlet width D and the half-angle β of the funnel as shown in Fig. 1(b). The Lexan plane forms an angle θ with the horizontal plane so the balls flow through the funnel into a collection container (E). A Plexiglas plate was placed on top of the aluminum walls to keep the flow in a single layer. The walls were grounded and the Lexan plane was treated with antistatic spray to minimize buildup of static electricity. After every 15 min of experiments the system was emptied and the surfaces were cleaned.

During a run the reservoir was kept above a certain level by regularly recycling balls from the collection container. As in an hourglass, it was found that the level of balls in the reservoir did not affect the funnel flow.

The inclination angle θ and the funnel parameters D and β are the control parameters of the experiment. Variation of β has been found by VD [5] to produce the most interesting changes in the flow properties. Thus D and θ were kept fixed at 10.0 mm and 4.1°, respectively, unless stated otherwise.

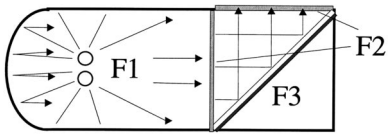

FIG. 2. Cross section of the light supply.

The angle β was varied in the range $0° - 3°$. In the funnel a coordinate system was used where x signifies the distance from the funnel outlet ($0 < x < 200$ cm). The uncertainty in determining β, D, and θ was approximately $\pm 0.01°$, ± 0.1 mm, and $\pm 0.05°$, respectively. It was also found that the local value of θ could deviate from the mean by as much as $\pm 0.4°$ since the plane was not perfectly rigid and was only supported at three points.

The system is not sealed, so there is no counterflow of air. The effect of the interstitial air has been estimated by VD [5] to be negligible except possibly for the highest observed ball velocities (~ 100 cm/s) where turbulence may become relevant.

B. Measurement system

Elements of the data acquisition system are also shown in Fig. 1(a). A light box (F) was placed below the lower 120 cm of the experiment. A cross section of this light source is shown in Fig. 2. It contained four 58 W fluorescent light tubes (F1) driven by a 40 kHz power supply. The light exits through two 20-cm-wide, sequentially placed mat glass plates (F2). The light path is extended to 45 cm by a mirror (F3). Most inner surfaces are reflecting. The box was equipped with a fan to avoid possible heat buildup, but due to the high efficiency of the tubes ($\sim 95\%$) this proved not to be a problem. A high-frequency power supply was chosen to minimize interference with the camera frame rate. (The shortest exposure time was 1 ms.) A fluorescent tube source was chosen for its spatially homogeneous illumination.

A video camera (G) [see Fig. 1(a)] was placed above the lower part of the funnel. Its analog output signal (H) was sent to a frame grabber in a PC (not shown). The camera was mounted on a stiff bar (I) and could be moved along its length. The bar was supported by a stabilized stand (J) (stabilization not shown) which could support weights over 100 kg. This oversized construction was necessary to prevent vibration of the camera. The inclination of the camera bar was adjustable so that it could be kept parallel to the flow plane. Thus the camera could be easily moved to different positions along the funnel without risking changes in distance and focus.

Observation of the flow in the lower 100 cm of the funnel was the primary focus. Some measurements were made in the upper 100 cm of the funnel with a different camera stand and the light box shifted accordingly. However, the shock waves there were mostly too dense and weak for reliable statistical analysis.

C. Video system

The video camera was a Pulnix TM-6701AN, 8 bit gray tone, noninterlaced, analog CCD camera. It is capable of filming 640×480 pixels at 60 frames/sec. The camera shutter may be adjusted from *no shutter* to 1/32 000 s. Shutter speeds of $0.5 - 1$ ms were mostly used given the available light intensity. The camera could be equipped with C-mount lenses. An 8 mm lens with a field of view of $\sim 40°$ was used.

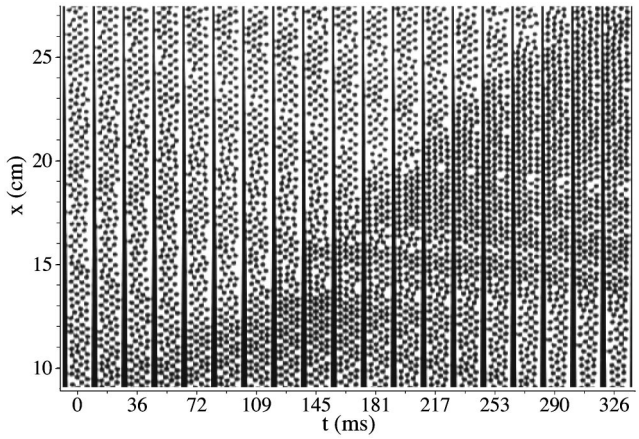

FIG. 3. Sequence of partial video frames showing a propagating shock ($\beta=0.3°$, $D=10$ mm, $\theta=4.1°$).

The camera was oriented such that the 640 pixel lines were parallel with the center line of the funnel. The term *view length* will denote the length of the funnel projected onto the 640 pixel axis of the camera. The 8 mm lens was mostly used at a height of ~ 136 cm giving a 100.2 cm view length as measured by a ruler on the flow plane. The aluminum walls and the area beyond them were painted black to ensure that only the flow area was illuminated from below. The balls therefore appeared as black ''dots'' on a white funnel region. Examples of single frames are shown in Fig. 3.

The analog output signal of the camera was not a standard video signal: it had a pixel rate of 25.5 MHz. This signal was transmitted to a Matrix Vision PCimage SGVS framegrabber card. This PCI-bus PC card has almost no internal memory and data are transmitted directly to the main memory of the PC. Up to 32 Mbytes may be grabbed per measurement.

Instead of grabbing full frames (or sections thereof), the lines of each incoming frame were summed in real time to avoid data overload. In other words, the light intensity of an image was averaged in the transverse direction to produce a 640-point one-dimensional measurement. More than 25 000 consecutive frames could be stored in this manner corresponding to almost 7 min of actual measurement time. These averaged frames are a measure of the local transverse averaged ball density but no longer allow identification of individual balls. They will henceforth be termed *density measurements*. An averaged series of empty funnel pictures was stored together with each measurement as a reference image.

These density measurements were converted into estimates of the *relative* granular density $\tilde{\rho}(x,t)$ by using the light intensities of an empty funnel and a fully packed funnel as reference points. (These estimated relative densities are subject to uncertainties arising from fluctuations in ball distributions.) The relative density $\tilde{\rho}(x,t)$ was not used for quantitative measurements but was well-suited for identifying and following density variations in space and time. Examples of data from density measurements are shown in Fig. 4. The contrast and offset of the gray scale digitalization are optimized to enhance the range of density variations in each measurement, which could depend strongly on the control parameters. Traveling shock waves are clearly recognizable as the dark stripes with positive slopes in Fig. 4. Raw gray scale plots of $\tilde{\rho}(x,t)$ will henceforth be referred to as *density maps*.

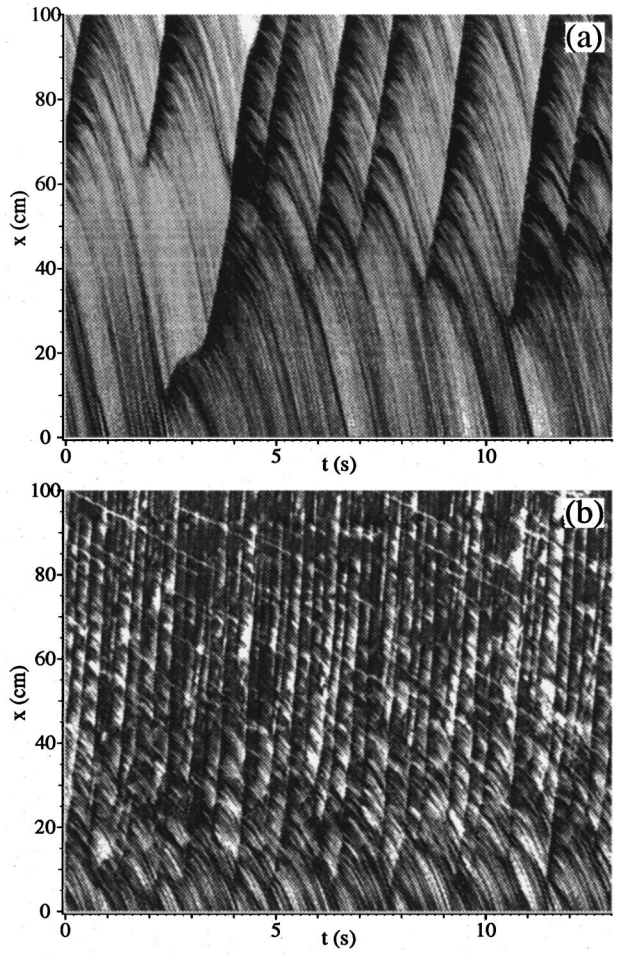

FIG. 4. Short sequence of density maps showing differences in shock wave frequency and velocity for (a) $\beta=0.1°$ and (b) $\beta=0.8°$ ($D=10$ mm, $\theta=4.1°$). Darker regions represent higher density.

IV. GENERAL BEHAVIOR

The density maps described in Sec. III C can be used to qualitatively characterize the different types of flow behavior.

A. Pipe flow ($0.0° \leqslant \beta < 0.1°$)

When the funnel walls are parallel or nearly parallel, the flow is relatively fast (~ 100 cm/s) and has a low average density ($\tilde{\rho} \sim 0.05-0.3$ except in shocks). The balls flow steadily out of the reservoir until they reach a certain point downstream where an almost stationary shock front occurs, as can be seen in Fig. 5(a). Its position depends on β. For $\beta=0°$ it occurs ~ 100 cm from the reservoir (i.e., about halfway down the funnel). When the funnel angle is increased to $\beta=0.075°$ it is only $20-40$ cm from the reservoir. Its position typically fluctuates $\pm 5-10$ cm.

In the meantime, relatively slow (~ 10 cm/s), large amplitude ($\Delta\tilde{\rho} \sim 0.5-0.8$) density waves (shock waves) origi-

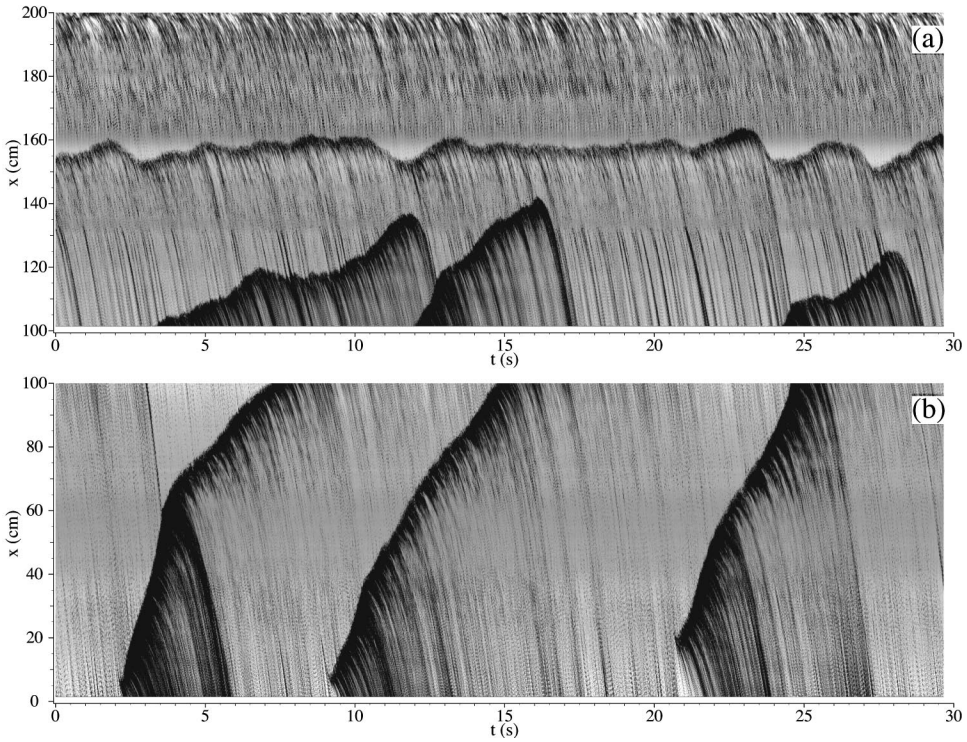

FIG. 5. Density maps showing pipe flow behavior at $\beta = 0.075°$ ($D = 10$ mm, $\theta = 4.1°$) in the (a) upper half and (b) lower half of the funnel.

nating from the lowest part of the funnel ($0-20$ cm from the outlet) propagate upstream against the flow as shown in Fig. 5(b). They are separated by time intervals of 5–60 s. (This time fluctuates strongly for all pipe flows but is shortest for $\beta \sim 0.075°$.) These shock waves usually stop and dissolve $10-40$ cm below the stationary shock. In any case, no shock waves ever reach the reservoir, which is therefore unaffected by events downstream. In particular, the flow rate is completely determined by the outflow from the reservoir [5].

In the pipe flow regime the balls move very fast and their motion is more likely to be influenced by irregularities in the funnel. For example, they are more likely to bounce and collide with the top plate. Such small perturbations in the flow caused by a submillimeter particle or a finger pressed against the top plate are sufficient to increase the local shock wave creation rate significantly. (Similarly, the position of the stationary shock can be moved upwards by applying pressure on the top plate with a finger.) In the pipe flow regime the system is therefore sensitive to the cleanliness of the system. Occasionally no shock waves can be observed at all (mostly at $\beta = 0°$ and mostly if the bottom plane or the balls are new, or if the top plane is elevated a few millimeters, or if the reservoir outflow is artificially reduced).

B. Intermittent flow ($0.1° < \beta < 0.5°$)

As β is increased from 0.1° to 0.4°, the shock wave speed increases from ~ 50 cm/s to ~ 150 cm/s while the time interval between shocks decreases from ~ 2 s to 0.5–1 s as shown in Figs. 6(a) and 6(b). Most shocks are created relatively close to the outlet, although, as will be shown later, there are, in fact, distinct shock creation sites throughout the full length of the funnel. Now almost all shock waves propagate as far as the reservoir as shown in Fig. 6(c).

Due to the lower ball velocities as compared with pipe flow, the flow is no longer very sensitive to irregularities in the surfaces or the cleanliness of the system. The flow behavior is therefore quite reproducible, except for a 20–60 s transient state after the flow is started.

The density fluctuations in the intermittent flow regime are smaller than for pipe flow. Inside a shock wave, the balls are nearly close-packed ($\tilde{\rho} \sim 1$). Between shocks $\tilde{\rho}$ may drop to 0.3–0.7. However, $\tilde{\rho}$ fluctuates only in the range 0.6–1.0 upstream close to the reservoir where the flow is even slower (5–20 cm/s).

C. Dense flow with density waves ($0.5° < \beta < 3.0°$)

In the dense flow regime the ball velocities are relatively low ($\lesssim 10-20$ cm/s). The transition from intermittent flow to dense flow is not sudden as β is increased (as opposed to the transition from pipe flow to intermittent flow where the shock waves reaching the reservoir make a significant difference in average density, average ball speed, shock frequency, and shock speeds). In this regime the flow is slower and almost uniformly dense (nearly close-packed with some defects). The shock waves are diminished in amplitude but they travel faster with increasing β as shown in Fig. 7. Near the reservoir the flow is so dense and slow that shock waves can no longer be resolved above $\beta \sim 0.7°$ (ball tracking based measurements indicate that they may, in fact, cease to exist [6]). This apparent shock-free zone extends further and further downstream as β is increased above $\beta \sim 0.7°$.

Above $\beta \sim 2.0°$ shock waves are no longer visible by eye anywhere in the funnel. However, they can still be discerned with image analysis methods involving ball tracking and in fact extremely weak shock waves persist near the outlet up to $\beta \sim 3.0°$ [6].

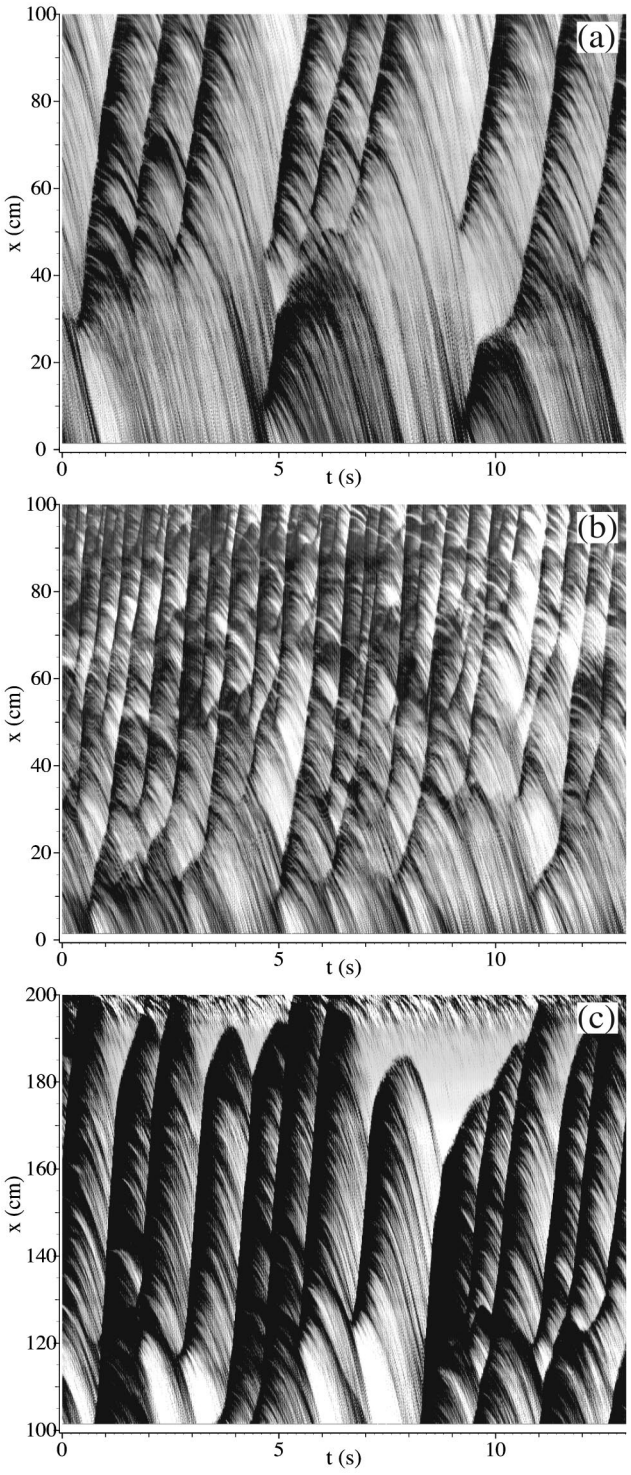

FIG. 6. Density maps showing intermittent flow behavior in the lower half of the funnel for (a) $\beta=0.1°$ and (b) $\beta=0.4°$, and (c) in the upper half of the funnel for $\beta=0.1°$ ($D=10$ mm, $\theta=4.1°$).

The dense flow regime is even less sensitive to external conditions than the other regimes. For $\beta \gtrsim 0.8°$ the flow no longer interacts with the top plane and it can be removed without affecting the flow. It is known that the average flow rate scales as $Q \propto D^{3/2}\beta^{-1/2}$ [5,18,21] for dense flows. In our system it was determined experimentally that $Q \propto D^{1.4}\beta^{-0.4}$ in the dense flow regime [5].

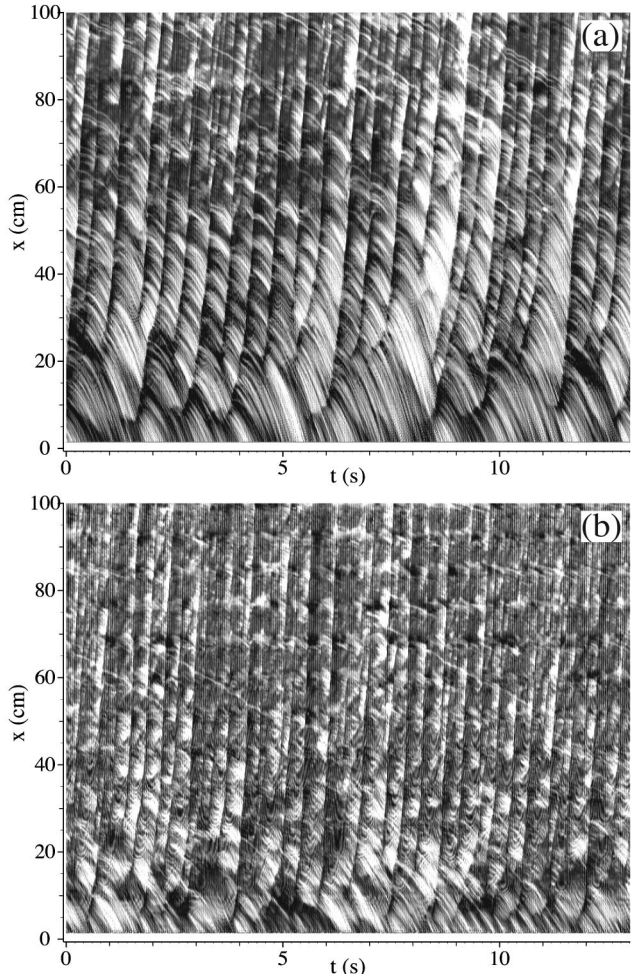

FIG. 7. Density maps showing dense flow behavior for (a) $\beta=0.6°$ and (b) $\beta=1.0°$ ($D=10$ mm, $\theta=4.1°$).

D. Monodispersity effects

Monodisperse spheres were chosen for experimental simplicity and convenience. However, this property affects the manner in which the balls can order, which we will now discuss.

As has been mentioned earlier, the balls tend to form close-packed triangular lattices inside a shock wave (and in other dense flow types) where the funnel geometry allows it. This is evident in Fig. 8. The lattice is always aligned with a lattice vector parallel to a wall. Since β is always small, a lattice vector is essentially parallel to the funnel axis. The geometry is shown in Fig. 9. The width of a triangular lattice with i rows is $W_i=2r+\sqrt{3}r(i-1)$, where r is a ball radius. The funnel width is $w(x)=D+2x\tan\beta$.

We might therefore expect that when $W_i=w(x)$ at special positions $x=\chi_i$ called packing sites, a monodisperse flow will be especially sensitive to the geometry. This condition gives us

$$\chi_i=\frac{2r+\sqrt{3}r(i-1)-D}{2\tan\beta}. \tag{1}$$

The packing sites are periodic with period

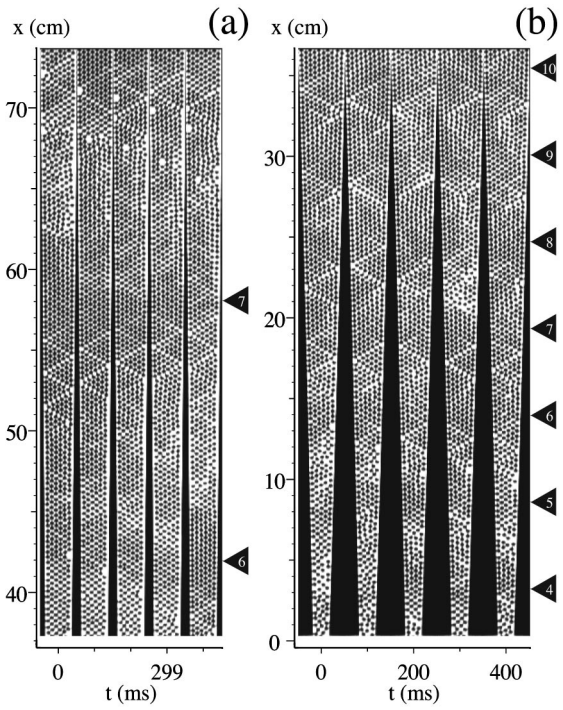

FIG. 8. Video frame sequences for (a) $\beta=0.5°$ and (b) $\beta=1.5°$. Triangular packing is clearly visible. (The black triangles at the right indicate the packing sites χ_i.)

$$\Delta\chi=\frac{\sqrt{3}r}{2\tan\beta}. \tag{2}$$

Thus the simplest way of identifying *any* packing site related effect is to look for periodic patterns along the length of the funnel.

Observations indicate that the balls keep rolling slowly even when packed by a passing shock. Thus each ball occupies slightly more space in a lattice than its physical radius would indicate. We expect then that the measured radius deduced from Eq. (2) might be slightly larger than the physical radius r.

V. SHOCK WAVE IDENTIFICATION METHODS

The study of shock waves or similar density fluctuations is usually limited to visual observation of their existence and propagation direction. (See, for example, Refs. [15,16,10].) Baxter and Behringer [17] made detailed measurements of the shock position as a function of time, but no systematic shock statistics were measured. Raafat *et al.* [12] and VD [5] measured average shock wave velocities using two-point measurements. However, in none of these experiments is it possible to study shock wave creation and velocity and frequency distribution characteristics.

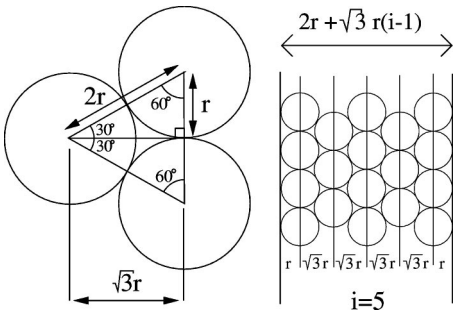

FIG. 9. Triangular packing structure showing $i=5$ rows of balls with radius r at the packing site χ_5.

Two specialized image analysis routines were developed to measure shock wave statistics, specifically the distributions of shock wave velocities, frequencies, and both positions and times of shock creation. A description of their basic principles and the general properties of their output follows below. A more detailed description can be found in Ref. [6].

A. Discontinuity tracking

The discontinuity tracking (DT) method is based on the following assumptions concerning shock wave properties.

(i) Once created, shock waves propagate upstream to the end of the view length. They do not disappear on the way.

(ii) At any given position, consecutive shock waves are separated by at least 0.1 sec.

(iii) The shock is represented by a relatively rapid temporal density increase at each point it passes — except for length intervals $\lesssim 5$ cm.

The last assumption reflects the fact that shock waves pack incoming balls. This packing may contain defects. These defects will appear as holes in the average density, and thus the temporal density increase will be shifted or absent at certain positions.

The algorithm does the following: All temporal density increments above a certain threshold farthest upstream are taken to be potential shock waves. The routine attempts to trace temporal density increments backwards in time and downwards in x. If the tracing cannot continue at a point, it tries a ''small jump'' to a suitable temporal density increment at some lower position. If no new suitable density increment can be found, a sequence of larger jumps is attempted. If a jump is approved, the tracing continues. If not, the last point is defined as the beginning of the shock wave. These points are fitted with a high-order polynomial. In the end the shock wave positions are binned into 1.6 cm sections. For each position of the shock wave the time and the velocity (the derivative of the polynomial) are stored together with the average density increase and the number of registered shock points in a given bin.

In Fig. 10(a) a density measurement with a number of shock waves is shown. The points found in each shock wave (before the polynomial fit is performed) are shown in Fig. 10(b).

The ''choices'' of the algorithm are governed by a number of parameters (e.g., initial threshold, allowed jumping lengths). The settings of these parameters are adjusted and tested before each dataset is processed. The performance of the routine has been found not to depend strongly on the values of these parameters. A satisfactory parameter setting for a given data file usually performs reasonably well on data files with similar values of β, D, and θ.

The DT routine works reasonably well for $0.1°<\beta\leqslant 0.4°$. For higher β the performance becomes increasingly poor. For smaller β the shocks may occasionally pause or dissolve midway, causing the routine to miss the lower part of a shock wave.

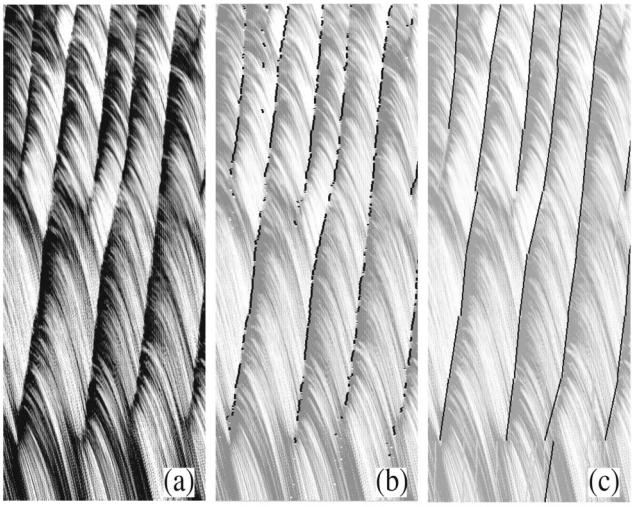

FIG. 10. Illustration of DT and GE methods of shock wave tracking for the same 5 s sequence in the lower 100 cm of the funnel ($\beta=0.2°$, $D=10$ mm, $\theta=4.1°$). (a) Density map. (b) ''Skeleton'' of points in DT method (polynomial not shown). (c) Line segments of GE 8 method.

B. Gradient edge detection

The gradient edge (GE) detection method is based on the assumption that a shock wave is an almost piecewise linear edge curve $x_S(t)$ in the $\tilde{\rho}(x,t)$ density map. [For fixed x the edge $x_S(t)$ has a sigmoidal profile but it is still locally approximately linear.]

The map is divided into a number of *strips*. (The strips are consecutive x intervals corresponding to 4, 8, or 16 equipartitions of the view length.) Through each strip a number of shock waves pass at certain times with certain velocities. Every *rising edge* in the density map that is encountered is fitted to a two-dimensional edge model function whose time and slope $u=dx_S/dt$ may be varied. The fits above a certain success threshold are registered as shock waves. Thus a number of shock wave arrival times τ_i and their velocities u_i are recorded for each x strip. (The value of x is taken to be the center of the strip.)

If sixteen strips are used, the x resolution is good, while the u determination is not. If four strips are used, the velocities are well determined, but the x resolution of the time interval between shock waves $\delta_i=\tau_i-\tau_{i-1}$ is less than satisfactory. (It will be shown later that the x dependence of the average time interval has interesting short length scale variations.) Eight strips therefore represent an acceptable tradeoff that is thus used most frequently. Data based on the GE method using 4, 8, or 16 strips will henceforward be denoted GE 4, GE 8, or GE 16, respectively. An example of the application of GE 8 is shown in Fig. 10(c).

Since no data are shared between strips, the presence or absence of gross discrepancies between the output data of neighboring strips gives an indication of the success or failure of the algorithm.

An important property of this routine is that it only measures the average time and velocity in a certain x strip. Knowledge of the past and future of the passing shock wave is not available. Thus statistics of, for example, shock wave creation positions are not possible.

For strips with virtually no shock waves (usually near the outlet) the routine may occasionally produce false shock waves. This tendency can be reduced significantly by tuning parameters, but if there are almost no real shock waves in the strip in question, the effect on the statistics of a few *''ghost shocks''* may be significant. Consequently the statistics of the strip closest to the outlet is the most uncertain since it has the fewest shock waves. [An example of a ghost shock can be seen in Fig. 10(c) in the bottom strip.]

Very fast shock waves are represented with almost vertical edges in the density maps $\tilde{\rho}(x,t)$. The slope of these edges is harder to determine than more moderate slopes. Consequently the uncertainty of high shock wave velocities is larger than that of moderate velocities.

C. Comparison of the two methods

The identification by eye of shock waves as global features in the $\tilde{\rho}(x,t)$ map is relatively easy. Locally [at some (x,t) position], however, it can be hard to define exactly which density fluctuations are passing shock waves and which are not. Visual observation is still the best guide and the DT method is designed to imitate the action of the human eye (and does so fairly successfully). It connects a number of noisy points into a global feature — fitting the concept of a shock wave. The performance of each algorithm has been visually verified to be quite good, but this should not be the only measure of performance.

The DT and the GE algorithms both work on the following assumptions.

(i) A shock wave is a curvelike feature in $\tilde{\rho}(x,t)$ with some extent in both x and t.

(ii) A shock wave is reasonably continuous with a well defined (not too fast varying) velocity.

(iii) A shock wave constitutes a (reasonably large and fast) temporal increase in the relative density $\tilde{\rho}$ in most points it passes.

Beyond this working definition of density shock waves, there are *no method similarities* between the two algorithms. Thus their results may be used for mutual control. The GE algorithm might seem preferable due to its conceptual simplicity and its applicability for a wide range of the funnel angle. However, the low x resolution of the routine and its inability to identify where a shock wave is created will later prove to be somewhat important. A detailed investigation of the properties of the resulting statistics of the GE and DT methods and a quantitative comparison of their properties can be found in the Appendix.

VI. SHOCK WAVE STATISTICS

In this section we present the dependence of the shock wave statistics on x and the experimental parameters. All data are based on the GE and DT methods. First the dependence of shock wave statistics on x and β is presented in Secs. VI A and VI B, respectively (both with $D=10$ mm and $\theta=4.1°$). The consequences of varying D and θ are discussed in Sec. VI C.

A. Dependence on x

DT based distributions of $u(x)$ are shown as contour plots in Figs. 11(a) and 11(b). The distributions seem to exhibit variations correlated with the packing sites χ_i. Below each packing site a higher number of low shock speeds is ob-

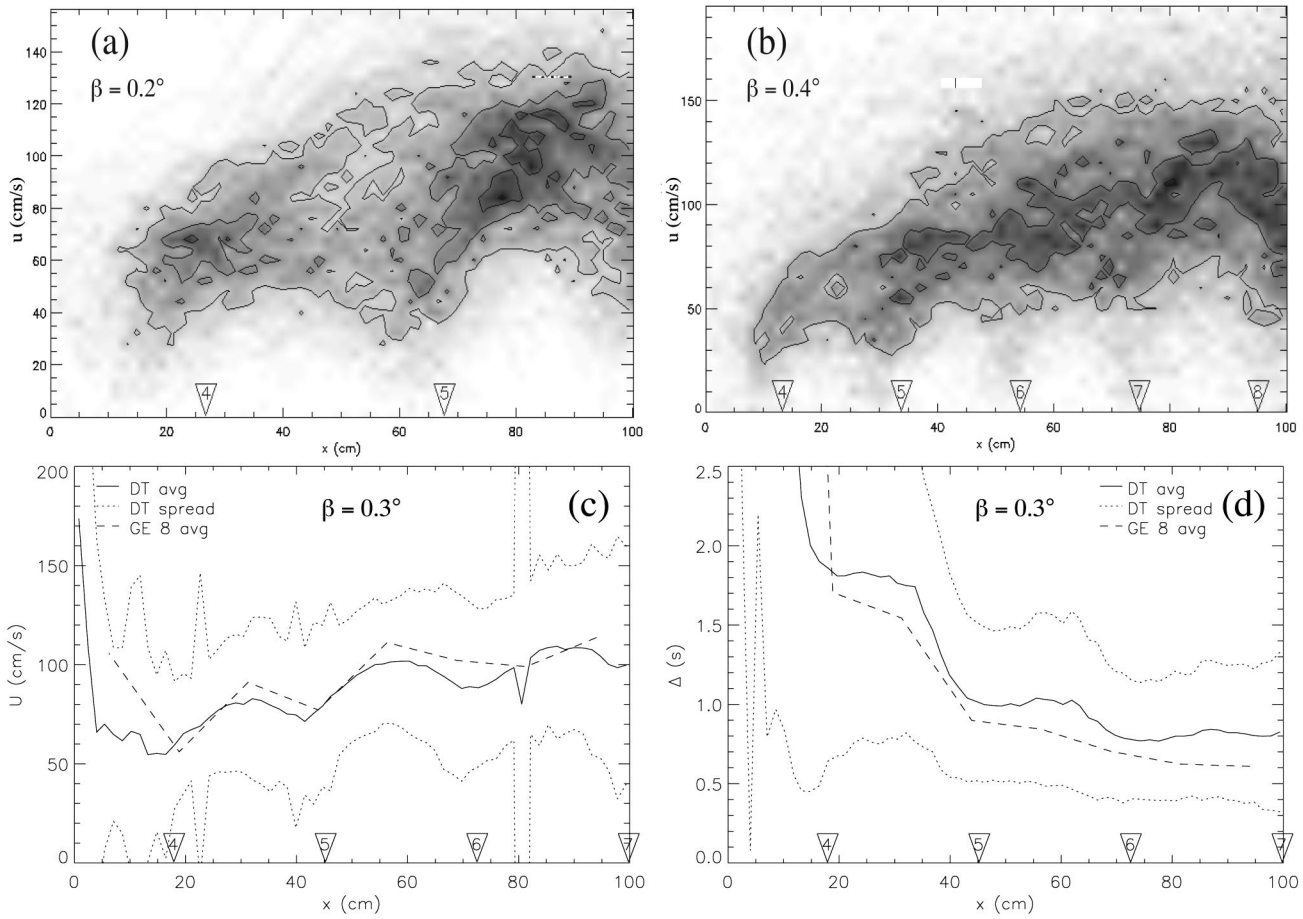

FIG. 11. The velocity distribution $u(x)$ (DT method) shown as a contour plot (darker = higher probability) for (a) $\beta=0.2°$ and (b) $\beta=0.4°$. Examples of the average velocity $U(x)$ and time interval $\Delta(x)$ are shown in (c) and (d), respectively. (The approximate spread of the distributions is also shown.) In all cases the influence of the packing sites χ_i (shown as inverted triangles) is clearly visible.

served and an associated broadening in the distribution is seen. Furthermore, the distributions of $u(x)$ exhibit a general increasing trend as one moves upstream. Aside from these variations, the distributions do not have significant structures.

The average velocity $U(x)=\langle u(x)\rangle$ shown in Fig. 11(c) is just as informative and more useful. Note that it shows the same packing site related variations and general increasing trend as the distribution $u(x)$ itself. Thus, from now on, we will only discuss the average values of the various distributions rather than the distributions themselves.

The average time interval between consecutive shocks $\Delta(x)=\langle\delta(x)\rangle$ is shown in Fig. 11(d). It exhibits a pronounced set of steps downwards just at or below the packing sites, corresponding to a growing frequency of shock waves. Between the packing sites $\Delta(x)$ seems reasonably constant.

Figures 11(c) and 11(d) also reveal how the limited spatial resolution of GE based $U(x)$ and $\Delta(x)$ statistics makes it hard to study the packing site periodicity. The general trend for $\beta\leqslant 0.4°$ seems to be that $U(x)$ temporarily drops slightly just below each packing site and that $\Delta(x)$ decreases in steps centered at or just below each packing site. There is no reason to assume that this behavior does not continue to some extent for $\beta>0.4°$, but here only GE based statistics are available and the periodicity cannot be resolved.

Any packing site periodicity must be assumed to be a consequence of the monodispersity of our system (see Sec. IV D). Spatial large scale trends of $U(x)$ and $\Delta(x)$, on the other hand, may reveal properties of a more general nature. Thus the possible packing site periodicity and the large scale trends are discussed here separately.

As discussed in Sec. IV B, almost no shocks are observed to disappear on their way up through the funnel. Consequently, the stepwise drop in the time interval $\Delta(x)$ must be associated with many new shock waves around packing sites and few elsewhere. This pattern may well be the most important consequence of monodispersity and is investigated more thoroughly later.

Having established the nature of the packing site related variations of $U(x)$ and $\Delta(x)$, we will now investigate their large scale dependence on x. This can be done by using GE 4– and GE 8–based statistics. In Figs. 12(a)–12(c) the average shock wave velocities $U(x)$ are shown for the full range of available values of β for $x<100$ cm. Generally $U(x)$ is observed to increase with both x and β. For $\beta<0.15°$, $U(x)$ seems roughly constant, but since $\Delta\chi_{\beta=0.1°}=81$ cm, the packing site variations and general increasing trend do not have much meaning. The values of $U(x)$ seem consistently lower for $\beta=0.125°$ than for $\beta=0.1°$ or $\beta=0.15°$. The reason for this is not clear.

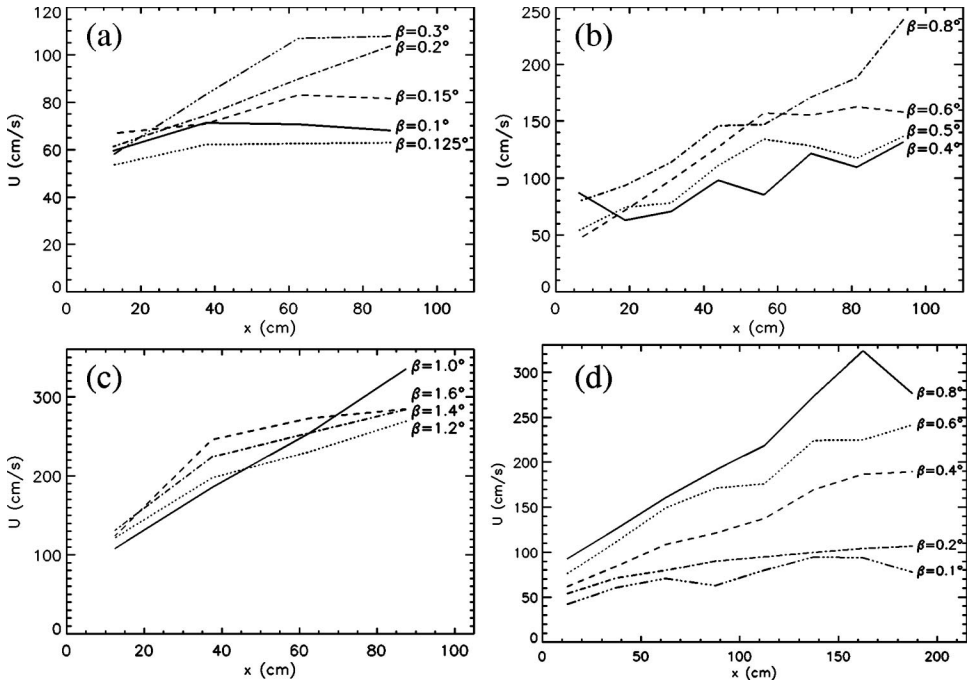

FIG. 12. Large scale dependence of $U(x)$: (a) $0.1° \leqslant \beta \leqslant 0.3°$ (GE 4 method), (b) $0.4° \leqslant \beta \leqslant 0.8°$ (GE 8 method), (c) $1.0° \leqslant \beta \leqslant 1.6°$ (GE 4 method). In (d) we show measurements for the full funnel length (which therefore consist of two separate data sets).

For $\beta > 1.0°$ and $x > 50$ cm, $U(x)$ appears to drop again. It was established in Sec. IV C that the shock amplitudes are very small in this regime and consequently the algorithm may have severe problems in identifying them. It seems likely (and has partially been confirmed by methods based on ball tracking [6]) that the growing trend in $U(x)$ continues as the amplitudes of the shocks vanish.

The vast majority of the data presented here are from the lower 100 cm of the funnel where most shocks are created and the phenomenology is most varied. Nevertheless, it is interesting to see what effects the proximity of the reservoir has on shock wave statistics. As discussed in Sec. IV C, the shock waves appear to become weaker and weaker as they approach the reservoir.

The resulting GE 4–based velocity statistics of the near-reservoir measurements (100 cm $< x <$ 200 cm) are shown in Fig. 12(d) combined with the statistics from the lower part of the funnel. The growth of $U(x)$ seems to continue throughout the length of the funnel for $0.2° \leqslant \beta \leqslant 0.6°$. For $\beta \geqslant 0.8°$ the shock waves are very hard to detect in the upper 100 cm of the funnel and the drop in $U(x)$ here is most likely a consequence of a partial inability of the algorithm to identify the shocks. For $\beta = 0.1°$, many of the shock waves vanish with their velocity approaching zero over a short distance for $x > 170$ cm as shown in Fig. 6(c). The GE 4 method is too coarse-grained to resolve this behavior, and thus only a small drop in $U(x)$ is observed.

The average time interval $\Delta(x)$ is observed to decrease for increasing x. This corresponds to a growth in the number of shock waves and thus the shock wave frequency $\nu(x) = \Delta^{-1}(x)$. In Fig. 13 the average shock frequency $\nu(x)$ is shown for different values of β. For the small β values in Fig. 13(a), a packing site related stepwise change is still observed. For $\beta \geqslant 0.5°$ [Fig. 13(b)], no further step behavior can be resolved – not even with GE 16–based statistics. The large scale behavior for $\beta \geqslant 0.3°$ seems to be a decaying growth throughout the lower 100 cm of the funnel. Figure 13(c) combines GE 8 statistics of the lower part of the funnel with measurements from the upper 100 cm. The curves for $\beta = 0.2°$ and $\beta = 0.4°$ show a continued decaying growth, too. For $\beta = 0.6°$ and $x > 100$ cm, many shocks go undetected by the GE algorithm due to very low shock amplitudes and certain experimental problems. This leads to an underestimation of the corresponding values of $\nu(x)$ in Fig. 13(c).

No values of $\nu(x)$ are shown for $\beta > 1.0°$ since only the most pronounced shock waves can be picked out by the routines (or the eye for that matter). Thus the registered number of shocks would reflect some density amplitude threshold rather than the actual number of shocks.

B. Dependence on β

In the section above it has been established that the average shock velocity $U(x)$ and shock frequency $\nu(x)$ both generally grow as a function of β at any point in the funnel. It would be convenient to get a better understanding of the nature of this growth. In Fig. 14(a) we show $U(x)$ at different sites along the length of the funnel. Apart from the dip at $\beta = 0.125°$ discussed earlier [see Sec. VI A and Fig. 12(a)], $U(x)$ is observed to increase as a function of β from 0.1° to 0.8°. For $x < 50$ cm this trend continues throughout the studied range. For $x > 50$ cm, the values at $\beta = 1.0°$ seem slightly too high and the subsequent data points display a drop off. This was also observed in Fig. 12(c) and has been discussed in Sec. VI A.

The growth of the shock frequency $\nu(x)$ is shown in Fig. 14(b). No data for $\beta > 1.0°$ or for $x > 100$ cm are presented due to the large systematic errors in these regimes. The shock waves seem to grow smoothly with increasing β at all four mapped sections of the funnel.

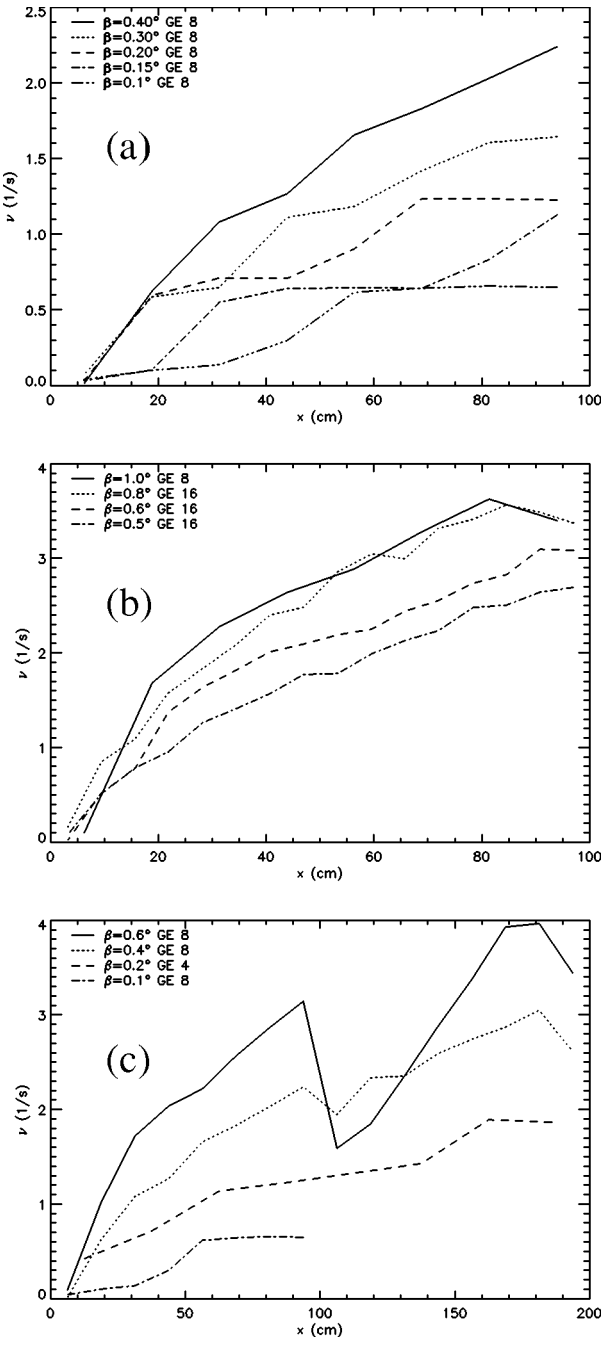

FIG. 13. Large scale dependence of $\nu(x)$: (a) $0.1° \leqslant \beta \leqslant 0.4°$, (b) $0.5° \leqslant \beta \leqslant 1.0°$. In (c) we show measurements for the full funnel length (which therefore consist of two separate data sets). The data for $\beta = 0.6°$ have large uncertainties (see text).

C. Dependence on D and θ

Since the recording, handling, and processing of the 32 Mbyte density data files are rather time consuming, only a limited number of measurements of sufficient length to give good statistics have been made (~ 55). The vast majority of these data sets have been recorded at $D = 10$ mm and $\theta = 4.1°$ since the β dependence of the dynamics has been the main focus of this project. To get a rough idea how the dynamics depend on D and θ, a few measurements have been made at $D = 7$ mm and $D = 14$ mm ($\theta = 4.1°$, $\beta \in \{0.1°, 0.4°, 1.0°\}$) and at $\theta = 3.0°$ and $\theta = 5.0°$ ($D = 10$ mm, $\beta \in \{0.1°, 0.2°, 0.4°, 0.6°, 1.0°\}$). The dependence of

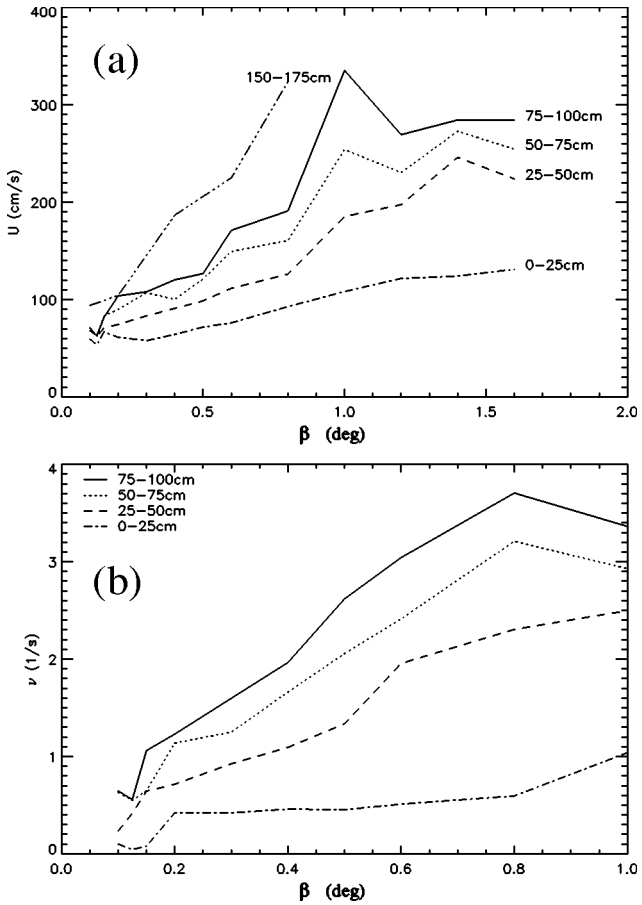

FIG. 14. Dependence of (a) $U(x)$ and (b) $\nu(x)$ on β (GE 4 method).

$U(x)$ and $\nu(x)$ on D is shown in Figs. 15(a) and 15(b), respectively, at $x \sim 63$ cm. The flow is generally denser with faster, more frequent shock waves for $D = 7$ mm. At $\beta = 1.0°$, the shock wave amplitudes are already too low for the GE algorithm to identify them accurately (thus the errors on these points could be $\pm 25\%$).

For $D = 14$ mm the flow is less dense with fewer, slower shocks. The borders between the different flow regimes appear to have moved accordingly. The change from *pipe flow* to *intermittent flow* seems to occur above $\beta = 0.1°$, causing $U(x)$ and $\nu(x)$ to drop below the values that might be expected. Generally both $U(x)$ and $\nu(x)$ for fixed x seem to decrease as functions of D.

As shown in Figs. 16(a) and 16(b), the θ dependence has been examined for more β values. There appears to be only a weak dependence of $U(x)$ and $\nu(x)$ on θ.

VII. RESCALING FUNNEL POSITION

Periodic variations of $U(x)$ with the packing sites (and thus the packing site index i) are displayed in Fig. 11 and discussed in Sec. VI A. The DT based averages are plotted as functions of a continuous version of the index variable

$$i = \frac{D + 2x \tan\beta - (2 - \sqrt{3})r}{\sqrt{3}r} \tag{3}$$

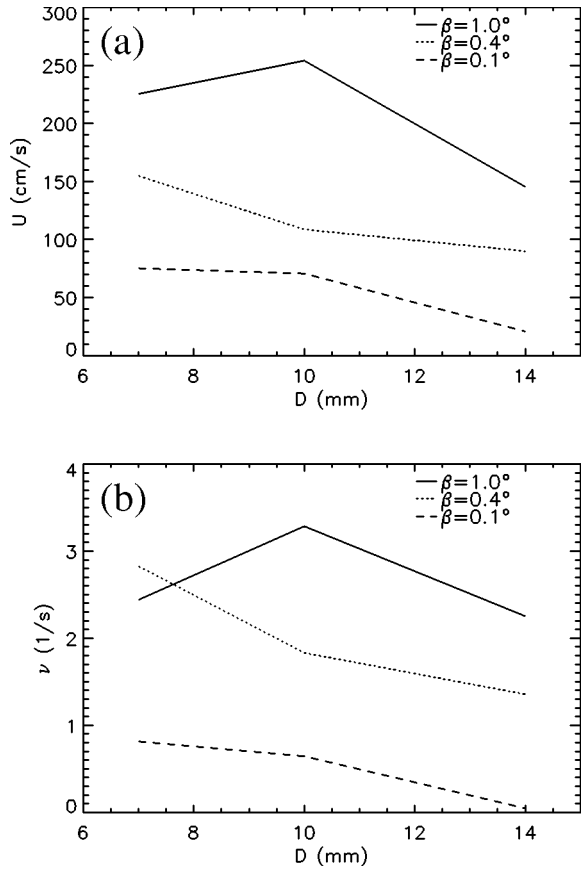

FIG. 15. Dependence of (a) $U(x)$ and (b) $\nu(x)$ on D (GE 4 method). (The data points for $\beta=1.0°$ and $D=7$ mm are highly uncertain due to low shock amplitudes.)

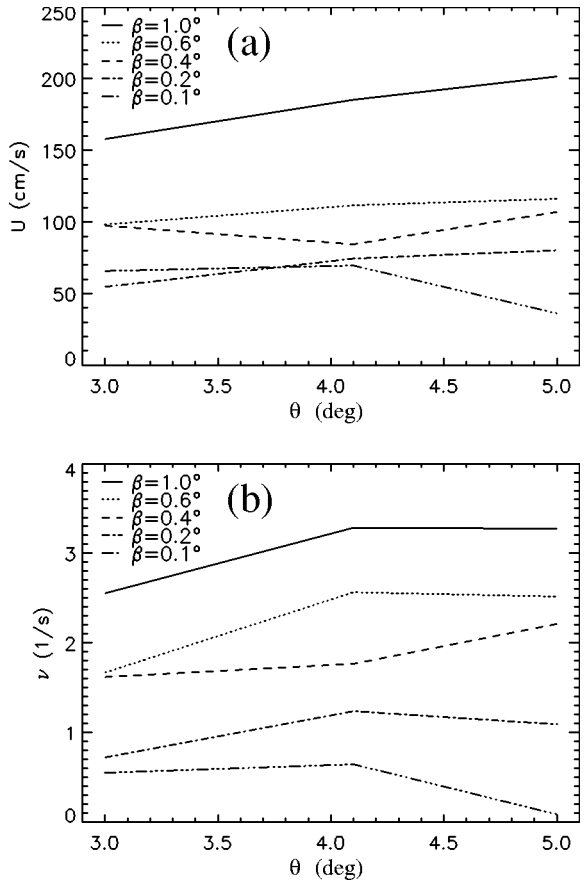

FIG. 16. Dependence of (a) $U(x)$ and (b) $\nu(x)$ on θ (GE 4 method).

as shown in Fig. 17(a). Not only are the phases and frequencies consistent, but most values of $U(x)$ seem to fall on the same curve (apart from the values at $\beta=0.4°$, where DT based analysis is most likely to have minor systematic errors anyway). The i rescaling is just a β-dependent rescaling of the x coordinates. Since the packing site indexing only makes sense for monodispersity effects, the equivalent funnel width is $w=D+2x\tan\beta$. The GE 4–based $U(x)$ statistics from Fig. 12(d) are replotted as functions of w in Fig. 17(b). Each data point is an average of local packing site variations such as those in Fig. 17(a).

It was then found that the slope for $D=7$ mm was roughly twice as large as for $D=14$ mm, with the data for $D=10$ mm lying roughly in the middle. Thus rescaling w with the outlet width D seems worthwhile. In Fig. 17(c) we show $U(x)$ for $D=7$ mm, $D=10$ mm (where not stated), and $D=14$ mm as a function of the rescaled variable $\tilde{w}=(w-D)/D$. It seems that $U(x)$ has a short length scale dependence on the absolute width w of the funnel and a large scale dependence on the relative width w/D. It is not known why this particular rescaling is successful. Note that in polar coordinates the ratio w/D is equivalent to r/r_0, where r_0 is the radial position of the funnel outlet.

It would be desirable to extend the data collapse in Fig. 17(c) to include the data made at different θ. However, the observed dependence on θ (if any) is too weak to suggest any simple rescaling procedure.

VIII. SHOCK WAVE CREATION

In Figs. 11, 13, and 21 it appears that the growth in the shock wave frequency is concentrated at certain small intervals below each packing site. Consequently, it seems likely that especially many shock waves are created in these intervals. The DT algorithm follows each shock wave backwards to its creation place. Thus it is possible to calculate statistics on the positions where shock waves are created.

In Figs. 18(a)–18(c) the shock creation position statistics are shown for $\beta=0.2°$, $\beta=0.3°$, and $\beta=0.4°$, respectively. Each peak corresponds to an x value just below a packing site χ_i. These statistics clearly document that monodispersity effects on the shock wave frequency statistics cannot easily be ignored. Figure 19 shows a return plot of the sequence of shock wave creations in Fig. 18(b). (The creation sequence is ordered by the *time of departure* from the field of view of each created shock.) It is fairly clear that alternate creations at the two lowest packing sites are very frequent, while two subsequent shock wave creations at the highest shock creation site are rather rare. Since the DT algorithm on which these data are based misses 10–15 % of the shocks for $\beta\geqslant 0.3°$, more elaborate creation sequence statistics cannot be reliably obtained. In many sequences of three or four observed shock creation sites, one shock was missed. This would clutter the statistics of such sequences.

IX. SHOCK WAVE INTERACTIONS

Most of the treatment of shock wave behavior in the former sections has focused on the behavior of individual

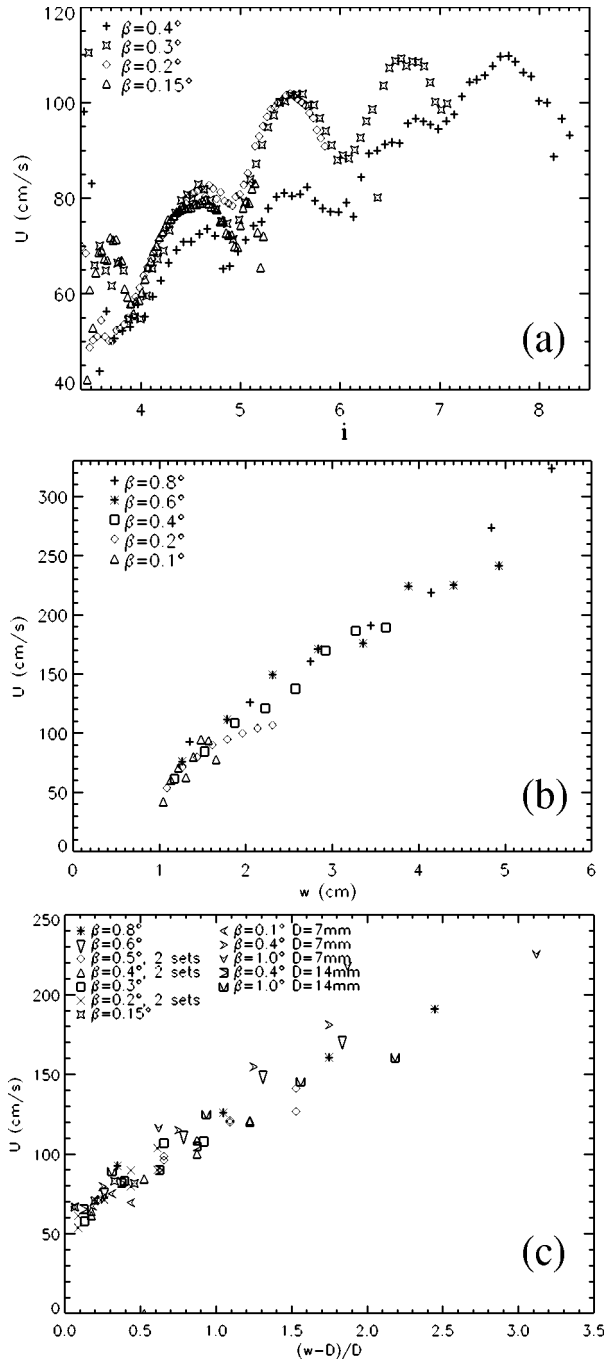

FIG. 17. Rescaling the shock position: (a) $U(x)$ versus packing site index i; (b) $U(x)$ versus funnel width w; (c) $U(x)$ versus the rescaled variable $(w-D)/D$ for $D=7$ mm, $D=10$ mm (where not stated), and $D=14$ mm. The error is roughly $\pm 10-30$ cm/s with increasing funnel width.

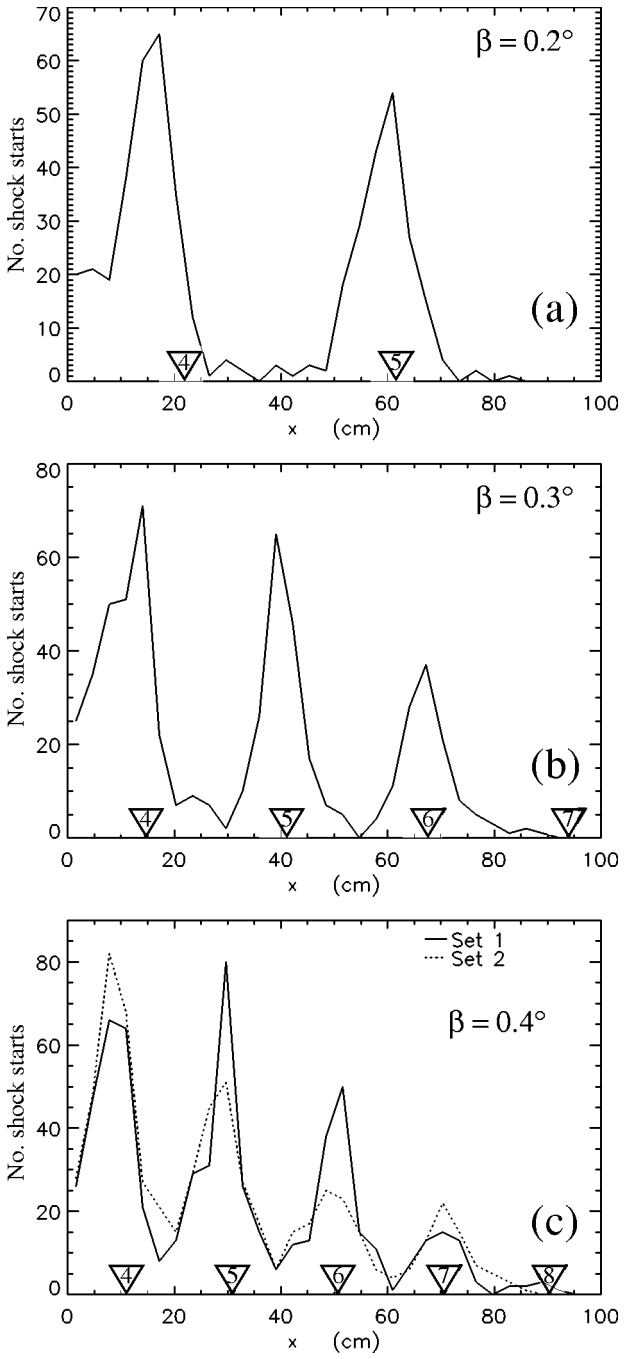

FIG. 18. Shock wave creation position statistics (DT method): (a) $\beta=0.2°$, (b) $\beta=0.3°$, (c) $\beta=0.4°$ (two measurements are shown). There are 32 points in each graph. The packing sites are marked with triangles on the x axis.

shock waves. The velocity and frequency of shock waves at any given point are given by distributions determined by β, D, and θ. However, it is clear that the propagation of a given shock wave is very dependent on the behavior of the shock waves upstream of it. This can be interpreted as an interaction between shock waves.

The best presently available tool for gaining insight into the nature of these interactions is the study of the density maps $\tilde{\rho}(x,t)$. As discussed in Sec. IV, patterns of downwards sloping stripes can be observed in the spaces between the shock waves in most $\tilde{\rho}(x,t)$ maps. The slopes of these stripes give an idea of the velocity of the balls at a given position. From the density maps we may possibly be able to make rough estimates of changes in velocity and density of the balls moving from one shock wave to another.

In Fig. 20 different examples of interesting shock wave propagation patterns are shown. In Fig. 20(a), two pseudo-stationary shock waves in pipe flow are seen. The shock at $x\sim 35$ cm has been stationary for ~ 50 s, in fact, but when another shock is created upstream of it, there is an apparent repulsive effect, and the older shock falls back and ''dies.''

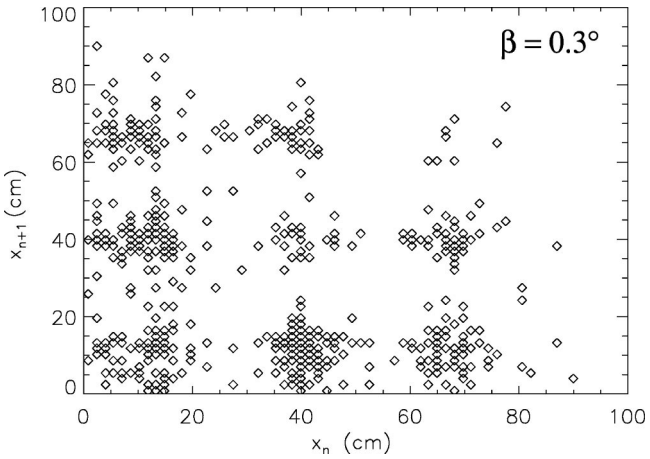

FIG. 19. Return plot of the shock wave creation position x_n in Fig. 18(b).

(It is generally observed that shock waves that propagate downstream are not very stable.)

In Fig. 20(b), a shock is created at P1. If this had not happened, the first balls caught in this shock would have arrived at the next shock with high speed at P2. This supply is temporarily cut off and the shock pauses until the new shock is well-established and starts having a steady outflow of balls from its downstream side. It thus seems that it is the creation more than the existence of a shock that has a repulsive effect on the shock coming after it at a lower position. This frequently observed interaction type is henceforward denoted *shock start repulsion*.

In Fig. 20(c), small fluctuations in the speed and density of balls leaving the downstream side of a shock at $t \sim 1.7$ s seem to play an important role in the creation of two new shock waves at P3 and P4. We denote this interaction type *shock seeding*. The last of these seeded shocks seems particularly pronounced and spurs a cascade of narrowly spaced shocks with low density amplitudes at P5 (this has not been observed for $D \geqslant 10$ mm). In Fig. 20(d), an example of two subsequent shock start repulsions is shown. Since the second starting shock seems to be a shock seeding of the first, this can be considered a three shock wave interaction. In Fig. 20(e), two weaker shock start repulsions are shown at $\beta = 0.4°$. Shock start repulsions are most frequently observed in the intermittent flow regime ($0.1° \leqslant \beta \leqslant 0.5°$). For $\beta \geqslant 0.3°$, the drops in $U(x)$ are usually less pronounced but persist over a larger x interval. Figure 20(f) shows an example of a weak shock traveling in front of a strong shock with a time interval $\leqslant 0.1$ s. We denote this shock type a *preshock*. Preshocks are only observed for $\beta \geqslant 0.4°$. Sometimes they are absorbed by the second shock and sometimes

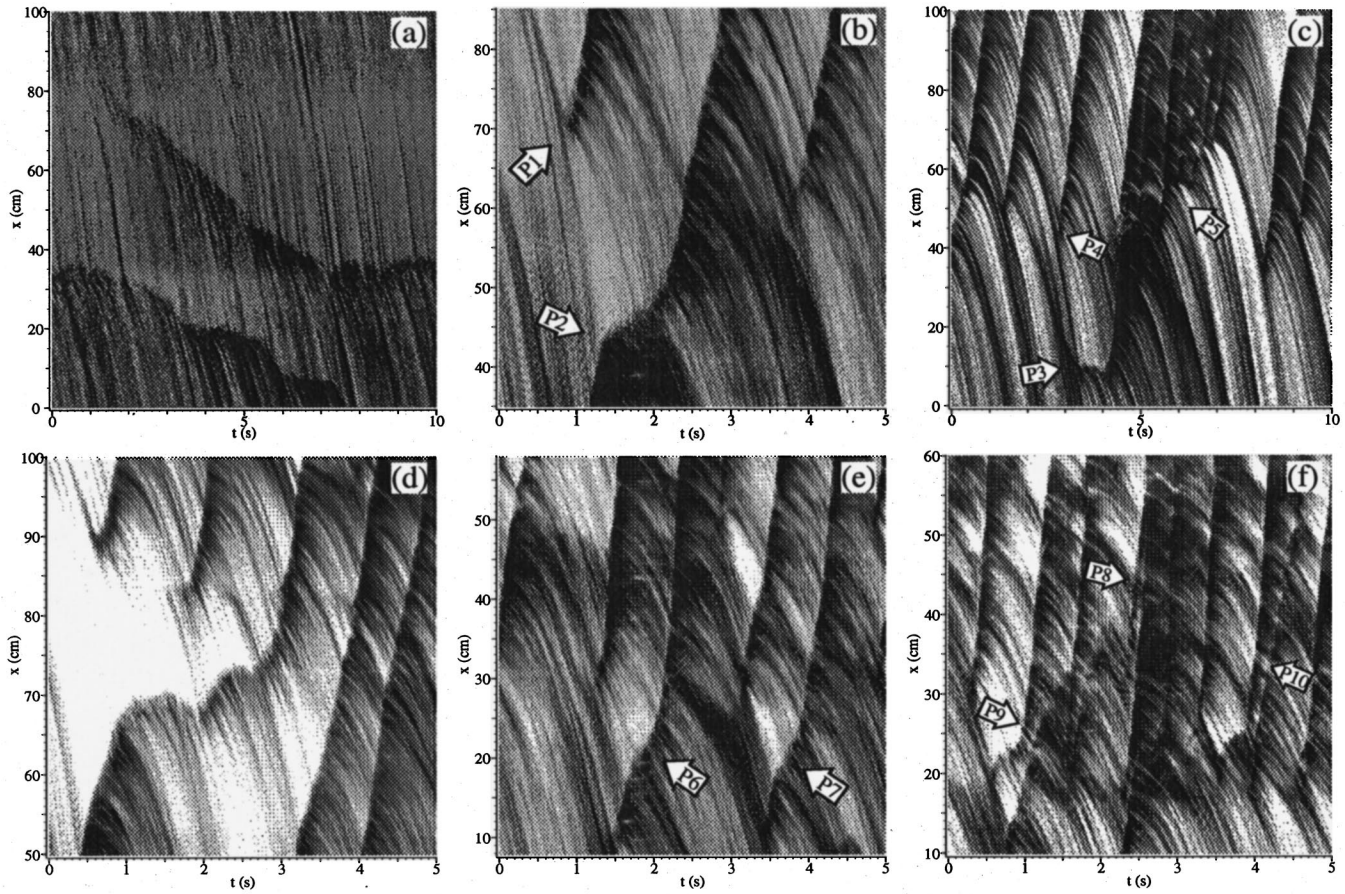

FIG. 20. Density maps $\tilde{\rho}(x,t)$ showing different examples of interactions. (a) Repulsion between nearly stationary shocks ($\beta = 0.0°$). (b) *Shock start repulsion* ($\beta = 0.1°$). (New shock P1 repels/delays shock coming from below at P2.) (c) *Shock seeding* at P3 and P4 and cascade of smaller shocks (P5) ($D = 7$ mm, $\beta = 0.1°$). (d) Two shock start repulsions ($\beta = 0.2°$). (e) Two separate weak shock start repulsions (P6 and P7) ($\beta = 0.4°$). (f) *Preshock* (P8) and *near-shock repulsion* (P9 and P10) ($\beta = 0.6°$).

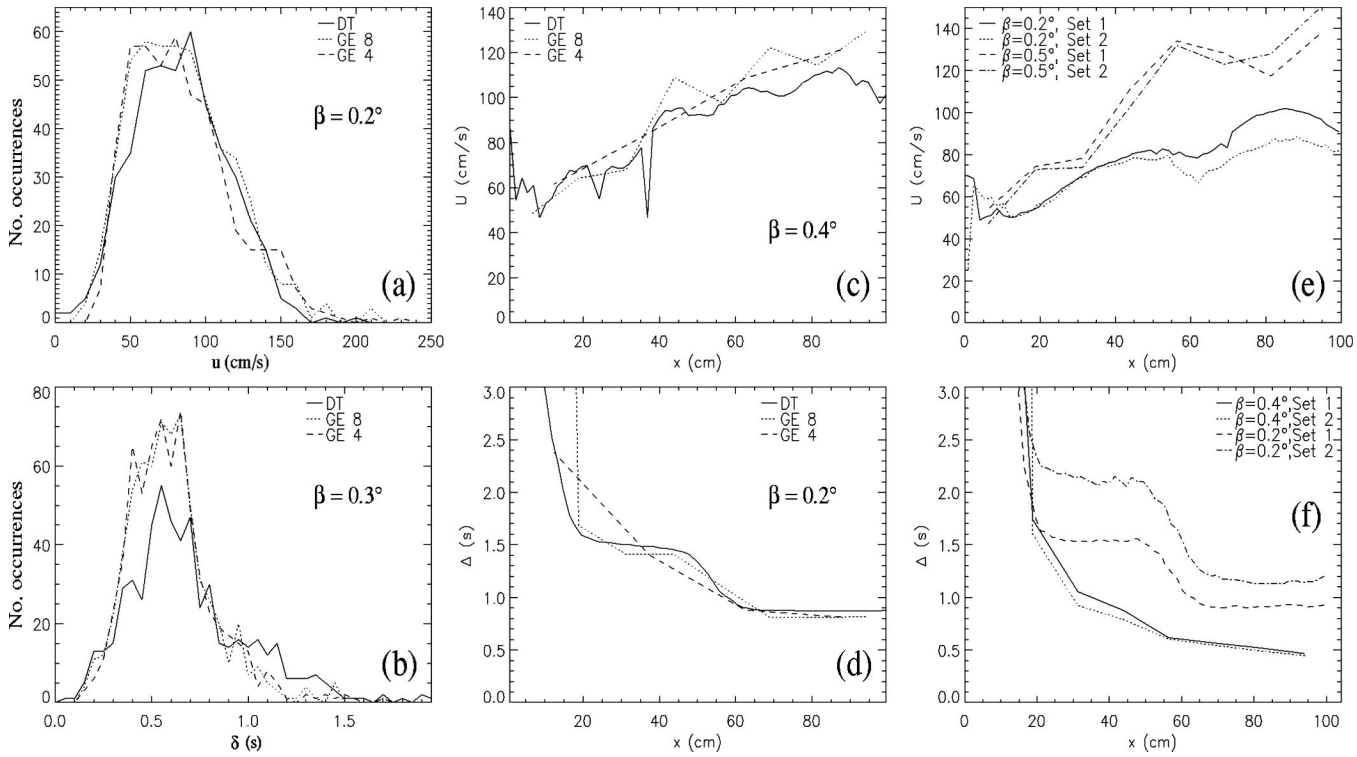

FIG. 21. Comparison of DT, GE 8, and GE 4 methods. (a) Distribution of $u(x)$ at $x\sim 70$ cm. (b) Distribution of $\delta(x)$ at $x\sim 70$ cm. (*No. occurrences* refers to number of observed shocks.) (c) Comparing $U(x)$. (d) Comparing $\Delta(x)$. (e) $U(x)$ at $\beta=0.5°$ (GE 8) and $\beta=0.2°$ (DT). (f) $\Delta(x)$ at $\beta=0.4°$ (GE 8) and $\beta=0.2°$ (DT). [The data in (e) and (f) compare two pairs of $U(x)$ and $\Delta(x)$ from data sets recorded on different days.]

they gain enough amplitude to repel the second shock. Preshocks frequently cause problems for the shock finding algorithms. Figure 20(f) also exhibits examples of other kinds of repulsions between shocks separated by small time intervals at P9 and P10. This interaction type is denoted *near shock repulsion* and is also only observed for $\beta\geqslant 0.4°$. Due to the limited temporal and spatial resolution of $\tilde{\rho}(x,t)$ measurements, it is hard to gain insight into the interaction mechanisms observed for $\beta\geqslant 0.4°$.

X. SUMMARY

We have presented the results of measurements of a granular flow of monodisperse metal balls in a two-dimensional funnel. The propagation of shock waves in this system using video-based spatio-temporal density measurements has been studied. By using two specialized image analysis tools, we have established the statistics of the propagation speeds of the shock waves and time intervals between consecutive shocks. The dependence of the shock waves on funnel angle, funnel outlet width, and flow plane inclination has been examined. In particular, we have found that the shock speed depends on the ratio between the local funnel width and the funnel outlet width. We have also established that new shock waves are created only at certain positions along the funnel as a consequence of the monodispersity of the granular matter. Finally we made qualitative observations of various types of interactions between shock waves.

ACKNOWLEDGMENTS

It is a pleasure to thank C. Veje for his assistance and insights and V. Putkaradze for many informative discussions. P.D. would like to thank Statens Naturvidenskabelige Forskningsråd (Danish Research Council) for support.

APPENDIX: DISCUSSION OF DT AND GE ALGORITHMS

During the ~ 7 min density measurements (see Sec. V) the number of shock waves passing any given position is between 200 and 1500. The time intervals between consecutive shocks $\delta(x)$ and the velocities of each shock $u(x)$ at the position are not constant as can be guessed from Fig. 6 and other plots of $\tilde{\rho}(x,t)$ presented here. The distributions of $u(x)$ and $\delta(x)$ based on the DT and GE algorithms are here compared and their reproducibility tested. We furthermore examine the strengths and weaknesses of the algorithms in order to determine which aspects of the statistics they each determine best.

In Figs. 21(a) and 21(b) we show examples of the DT and GE based distribution of $u(x)$ and $\delta(x)$. For the data of both methods the values of $u(x)$ and $\delta(x)$ are generally found to fall in distributions with standard deviations of the order of 25% to 50% of the average values. In Fig. 21(a) the distribution of $u(x)$ at $\beta=0.2°$ is shown using DT, GE 8, and GE 4 algorithms (see Secs. V A and V B). The distributions based on the different methods are roughly identical, somewhat asymmetric, and have a well defined peak region. In Fig. 21(b) the distributions of $\delta(x)$ are calculated using the DT, GE 8, and GE 4 methods at $\beta=0.3°$. The GE methods yields roughly identical results, while the DT method loses some shock waves. This causes lower values of $\delta(x)$ to be somewhat underrepresented while the larger values are overrepresented (corresponding to a double step). Generally the

DT method loses $0-5\,\%$ of the shocks for $0.1°<\beta\leqslant 0.2°$ and around $10-15\,\%$ for $0.3°\leqslant\beta\leqslant 0.4°$. For higher values of β the DT method is not used. The occasional missed shock wave does not seem to influence the $u(x)$ statistics of the DT method significantly.

In Figs. 21(c) and 21(d), $U(x)$ [the average of the $u(x)$ distribution] and $\Delta(x)$ [the average of the $\delta(x)$ distribution] are shown as functions of x for $\beta=0.4°$ and $\beta=0.2°$. The distribution averages based on the DT , GE 8, and GE 4 algorithms are compared. The DT method has a superior x resolution but displays occasional glitches. Apart from the inherent differences in x resolution, the algorithms give very similar results.

The flow dynamical features determined from the shock wave statistics are only interesting to the extent that they are reproducible. In Figs. 21(e) and 21(f), $U(x)$ and $\Delta(x)$ are shown. Each plot shows two pairs of average curves taken at two different days at the same parameter settings. The DT algorithm may be more sensitive to variations in light conditions and camera setting from day to day. Generally $u(x)$ statistics appear to have a slightly better reproducibility than $\delta(x)$ statistics. Alterations in the lighting conditions determine the contrast in observable density variations. Some shock waves with too weak apparent amplitudes will not be detected. Small changes in the lighting conditions affect the observed numbers of shocks and thus $\Delta(x)$. The statistics of $u(x)$ [and thus $U(x)$] is not strongly affected since the apparent amplitude and the speed of a shock seems rather independent.

Statistics based on GE 16 are not shown in Fig. 21. This algorithm has an unsatisfactory resolution in the determination of $u(x)$ and the statistics of $\delta(x)$ are plagued with too many false shock findings for $\beta<0.4°$ and too few found shocks for $\beta\geqslant 1.0°$. Statistics of GE 16 are satisfactory (and similar to GE 8) in the range $0.5°\leqslant\beta\leqslant 0.8°$.

The values of $\Delta(x)$ can be observed to diverge as $x\rightarrow 0$ cm in Figs. 21(d) and 21(f). This happens because there are very few observed shock waves near the outlet [see Figs. 6(a) and 6(b)]. Due to the low number of shocks, the statistics of both $u(x)$ and $\delta(x)$ are less reliable in this region as can be seen in Figs. 21(c) and 21(e). The divergence of $\Delta(x)$ is sometimes inconvenient in plots and the average shock wave frequency $\nu(x)=\Delta(x)^{-1}$ will partially be used instead of the average time between shocks.

Figures 21(c)–21(f) exhibit both an overall growth/decline [for $U(x)$ and $\Delta(x)$, respectively] and a periodic spatial variation with periods similar to the packing site periodicity to be expected for these values of β ($\Delta\chi_{\beta=0.2°}=40.3$ cm, $\Delta\chi_{\beta=0.3°}=26.9$ cm, and $\Delta\chi_{\beta=0.4°}=20.2$ cm using $\tilde{r}=1.625$ mm). Before entering an investigation of the nature of these possibly separate variation types, it is necessary to review the spatial resolutions of the algorithms and to compare them with the expected length scales of packing site periodicity. The DT method has a specified spatial resolution of ~ 1.6 cm (see Sec. V A). The GE n algorithms are subdivisions of 100 cm into n strips and consequently the spatial resolutions of GE 4, GE 8, and GE 16 are 25 cm, 12.5 cm, and 6.3 cm, respectively. From Eq. (2) we have $\Delta\chi\propto\beta^{-1}$ (for small β).

In order to measure a given periodic variation, a measuring resolution of at least twice the period must be used (similar to the notion of *Nyquist frequency*). Consequently, all the available algorithms will fail to register packing site variations above a certain value of β. Using Eq. (2) and the resolutions mentioned above, we get that GE 4 fails for $\beta>0.15°$, GE 8 fails for $\beta>0.3°$, GE 16 fails for $\beta>0.6°$, and DT fails for $\beta>2.0°$. The DT algorithm does not work for other reasons for $\beta>0.4°$ and GE 16 is only reliable for measurements of Δ for $0.5°<\beta<0.8°$.

Packing site periodicity in $U(x)$ is measurable for $0.1°\leqslant\beta\leqslant 0.4°$ and the DT algorithm gives the best resolution. The same holds for $\Delta(x)$ except for the possibility that GE 16 may be used to extend the range to $\beta=0.6$.

The failure to identify packing site periodicity of GE 4 and GE 8 in the majority of their regimes of validity does not render these routines useless. For values of β up to twice the failure values given above, their statistics may still be influenced by packing site periodicity [an effect equivalent to the *aliasing* effect of frequencies above the Nyquist frequency in Fourier transforms of unfiltered input (see Ref. [22])], but mainly the packing site effects will be averaged out. Thus GE 4 and GE 8 are well-suited for the study of variations over longer length scales.

[1] R. L. Brown and J. C. Richards, *Principles of Powder Mechanics* (Pergamon Press, Oxford, 1970).

[2] H. M. Jaeger and S. R. Nagel, Science **255**, 1523 (1992).

[3] H. M. Jaeger, S. R. Nagel, and R. P. Behringer, Rev. Mod. Phys. **68**, 1259 (1996).

[4] G. Hagen, Monatsber. Dtsch. Akad. Wiss. Berlin, S35 (1852); H. A. Janssen, Z. Ver. Dtsch. Ing. **39**, 1045 (1895).

[5] C. T. Veje and P. Dimon, Phys. Rev. E **54**, 4329 (1996); C. T. Veje, Master's thesis, University of Copenhagen (1995).

[6] S. Hørlück, Master's thesis, University of Copenhagen (1997).

[7] A. A. Mills, S. Day, and S. Parkes, Eur. J. Phys. **17**, 97 (1996).

[8] K. L. Schick and A. A. Verveen, Nature (London) **251**, 599 (1974).

[9] X. Wu, K. J. Måløy, A. Hansen, M. Ammi, and D. Bideau, Phys. Rev. Lett. **71**, 1363 (1993).

[10] T. Pöschel, J. Phys. I **4**, 499 (1994).

[11] C. T. Veje and P. Dimon, Phys. Rev. E **56**, 4376 (1997).

[12] T. Raafat, J. P. Hulin, and H. J. Herrmann, Phys. Rev. E **53**, 4345 (1996).

[13] A. Nakahara and T. Isoda, Phys. Rev. E **55**, 4264 (1997).

[14] R. P. Behringer and G. W. Baxter, in *Granular Matter—An Interdisciplinary Approach*, edited by A. Mehta (Springer-Verlag, Berlin, 1994), Chap. 3.

[15] J. Lee, S. C. Cowin, and J. S. Templeton, Trans. Soc. Rheol. **18**, 247 (1974).

[16] R. L. Michalowski, Powder Technol. **39**, 29 (1984).

[17] G. W. Baxter, R. P. Behringer, T. Fagert, and G. A. Johnson, Phys. Rev. Lett. **62**, 2825 (1989).

[18] R. L. Brown, Nature (London) **191**, 458 (1961).
[19] C. Brennen and J. C. Pearce, J. Appl. Mech. **45**, 43 (1978).
[20] G. H. Ristow and H. J. Herrmann, Phys. Rev. E **50**, 5 (1994).
[21] W. A. Beverloo, H. A. Leiger, and J. van de Velde, Chem. Eng. Sci. **15**, 260 (1961).
[22] W. H. Press, S. A. Teukolsky, W. T. Vetterling, and B. P. Flannery, *Numerical Recipes in C: The Art of Scientific Computing* (Cambridge University Press, Cambridge, 1992).